Orbital Motion Theory and Operational Regimes for Cylindrical Emissive Probes

Xin Chen 陈馨[1, a)] and G. Sanchez-Arriaga[1, b)]

Bioengineering and Aerospace Engineering Department,
Universidad Carlos III de Madrid, Leganes, Madrid 28911,
Spain

(Dated: 12 January 2017)

A full-kinetic model based on orbital-motion theory for cylindrical emissive probes (EPs) is presented. The conservation of the distribution function, the energy and the angular momentum for cylindrical probes immersed in collisionless and stationary plasmas is used to write the Vlasov-Poisson system as a single integro-differential equation. It describes self-consistently the electrostatic potential profile and, consequently, the current-voltage (I-V) probe characteristics. Its numerical solutions are used to identify different EP operational regimes, including orbital-motion-limited (OML)/non-OML current collection and monotonic/non-monotonic potential, in the parametric domain of probe bias and emission level. The most important features of the potential and density profiles are presented and compared with common approximations in the literature. Conventional methods to measure plasma potential with EPs are briefly revisited. A direct application of the model is to estimate plasma parameters by fitting I-V measurements to the theoretical results.

[a)]xin.chen@uc3m.es

[b)]gonzalo.sanchez@uc3m.es

I. INTRODUCTION

Sheath structure around an electron-emitting surface[1] is a fundamental problem in plasma physics with applications to dusty-grain[2] and spacecraft[3] charging, plasma boundary phenomena in fusion devices[4] and plasma thrusters[5], and bare thermionic tethers[6]. Emissive probe (EP), a hot cylinder emitting electrons, is of special importance because it is widely used as a plasma diagnostic tool[7–9]. This device was invented together with collective Langmuir probe (LP) in the early XX century[10,11]. The theoretical basis of the latter is now well-established[12–16]. However, due to the high complexity of emissive sheaths, a self-consistent kinetic theory for cylindrical EPs is not available yet.

For cylindrical LPs, Mott-Smith and Langmuir presented the orbital-motion-limited (OML) theory for current collection in 1920s[11]. For OML collection, the current is limited by the condition at the probe radius R, instead of that at an absorption boundary larger than R. Although their approach assumed an arbitrary separation between sheath and quasi-neutral plasma, lacking self-consistency, the OML theory may still be valid for small radius-to-Debye length ratios ($R/\lambda_{De} \ll 1$). In 1957, by considering only the radial motion of the attracted particles, Allen, Boyd and Reynolds (ABR)[17] found the radial potential distribution by solving a simple differential equation, with no division into sheath, presheath, and plasma regions. Although orbital motions were neglected in this theory, it still provides fairly good approximations for cold ion ($T_i \approx 0$) collection with spherical probes[18]. However, the ABR theory can not be applied for cylindrical probes due to the finite angular momentum, even for $T_i \approx 0$. This arises from the reason that the potential varies slower than $1/r^2$ in the cylindrical case[19]. Consequently, a more general theory is needed for cylindrical geometry.

This general theory for LPs arrived in the late 50s and early 60s, when the Orbital Motion Theory (OMT) was developed. As long as collisions, plasma drift, particle trapping, transient effects, and magnetic fields are not significant, the Vlasov equation conserves the distribution function $f_\alpha(\boldsymbol{r}, \boldsymbol{v})$, transverse energy E_α, and angular momentum J_α of each specie α. Particle densities $N_\alpha(r)$ can be written as functionals of the electrostatic potential $\phi(r)$ and, after substituting $N_\alpha(r)$ into Poisson's equation, it yields an integro-differential equation that describes self-consistently and rigorously the probe characteristic, i.e., the current-voltage (I-V) functional relation. Bernstein and Rabinowitz presented in 1959 an

elegant and self-consistency scheme for monoenergetic attracted particles. In 1964, Lam completed the theory by using boundary layer techniques in the limit of large probe radius ($R/\lambda_{De} \gg 1$) at high probe bias ($e\phi_p >> k_B T_e$, with T_e electron temperature and k_B the Boltzmann constant)[12]. In 1966, by solving the integro-differential equation numerically for a Maxwellian plasma, Laframboise calculated I-V characteristics for a vast range of probe and plasma parameters, within and beyond the OML regime[14].

To the knowledge of the authors, a general OMT for cylindrical EPs, being valid for arbitrary parameter values, has not been developed yet. Important theoretical difficulties arise for EPs due to the space-charge effects introduced by the emitted electrons. As thermionic emission is increased, for instance with probe temperature, the electron space charge grows and suppresses the electric field. At certain emission level, the electric field at the probe vanishes. Beyond it, a potential dip (or virtual cathode) develops adjacent to the probe and reflects a portion of emitted electrons back to the probe. The thermionic current is then said to be space-charge-limited (SCL) and appears to be limited by probe bias other than probe temperature. The sheath now is constituted by a negative-charge layer next to the probe and a positive-charge layer extending to the quasi-neutral plasma.

The SCL effect was first studied by Langmuir and his co-workers for single electron sheath[20] and for planar double sheath[21] in the 20s. Available analytical works on emissive sheaths commonly considered planar geometry[22–24]. Simulations also focused on planar[25–27] or spherical[3,28] sheaths. Among EP studies, orbital effects were usually ignored[29,30] or, if included, the analyses were limited to certain asymptotic cases. In the 70s, Chang et al.[31] studied the case for very large probe radius ($R >> \lambda_{De}$), assuming monoenergetic ions. Shortly after, Schuss and Parker[32] considered a situation in which not only an absorption radius does not exist for the ion collection at the probe radius R, but also there is no absorption radius for the ion collection at any radius larger than R. Numerical solutions of Poisson's equation for the virtual cathode in cylindrical geometry were found using an OML model, however with only emitted electrons considered[33]. Recently, by using boundary-layer techniques and kinetic modelling, a self-consistent asymptotic solution was found for OML condition at at high probe bias ($|e\phi_p| >> k_B T_e$)[34]. Without a rigorous and universal kinetic description for cylindrical EPs, a wide variety of methods exist - yet commonly with controversies - to infer plasma potential from experimental data[7]. Contrary to the successful application of the LP I-V curves from Laframboise to interpret plasma parameters[19], EP

techniques have not been used to infer other plasma parameters other than plasma potential.

This work presents the OMT for cylindrical EPs. Assuming the same hypothesis of the OMT for LPs, Section. II shows that the three conservation laws, f_α, E_α, and J_α, can also transform the Vlasov-Poisson system for cylindrical EPs into a single integro-differential equation, assuming half-Maxwellian emission and a Maxwellian plasma. Laframboise's theory for LPs can be recovered from our model by dropping the emission. The integro-differential equation governs cylindrical-EP characteristics rigorously and is used to calculate numerically the full I-V curves rapidly for different operational regimes, including positive/negative probe bias, monotonic/non-monotonic sheaths, OML/non-OML collection, and SCL/non-SCL emission. In Sec. III, the regimes are qualitatively discussed and identified in the parametric plane of probe bias and emission level. In Sec. IV, quantitative results on IV curves, operational regimes, potential/density profiles, and floating potentials are presented and discussed. The main conclusions, limitations of the OMT and future extensions of the theory are discussed in Sec. V.

II. ORBITAL MOTION THEORY FOR CYLINDRICAL EMITTERS

Let us consider a cylinder with radius R, bias ϕ_p relative to plasma, temperature T_p, and work-function W, emitting thermionic electrons at the surface with a density N_{emp}, and immersed at rest in a plasma with unperturbed density N_∞ and particle temperatures T_α ($\alpha = e, i$ for plasma electrons and ions). Plasma species are assumed to be Maxwellian at infinity, $f_\alpha(r \to \infty, v_r, v_\theta) = f_{M\alpha} \equiv \frac{N_\infty m_\alpha}{2\pi k T_\alpha} \exp\left[-\frac{m_\alpha}{2kT_\alpha}(v_r^2 + v_\theta^2)\right]$, with v_r and v_θ the radial and azimuthal velocities respectively. Emitted electrons are taken half-Maxwellian as $f_{em}(R, v_r > 0, v_\theta) = f_{HM} \equiv \frac{N_{emp} m_e}{\pi k T_p} \exp\left[-\frac{m_e}{2kT_p}(v_r^2 + v_\theta^2)\right]$. Following Richardson-Dushman (RD) law, electrons are emitted at the probe with the current per unit length being

$$I_{RD} = 2\pi R A_R T_p^2 \exp\left(-\frac{eW}{k_B T_p}\right), \tag{1}$$

where $A_R = 4\pi e m_e k_B^2/h^3 \approx 1.2 \times 10^6 A m^{-2} K^{-2}$ is a universal constant, h the Planck constant, and W the work function in eV. The HM distribution and RD law give the the emission level β as

$$\beta \equiv \frac{N_{emp}}{N_\infty} = \left(\frac{2\pi m_e k_B T_p}{h^2 N_\infty^{2/3}}\right)^{3/2} \exp\left(-\frac{eW}{k_B T_p}\right), \tag{2}$$

which depends on N_∞, T_p and eW/k_BT_p. Besides β, other relevant dimensionless parameters are

$$\delta_i \equiv \frac{T_i}{T_e} \ , \quad \delta_p \equiv \frac{T_p}{T_e} \ , \quad \varphi_p \equiv \frac{e\phi_p}{k_BT_e} \ , \quad \rho_0 \equiv \frac{R}{\lambda_{De}} \ , \tag{3}$$

with $\lambda_{De} = \sqrt{\varepsilon_0 k_B T_e / e^2 N_\infty}$ the plasma electron Debye length and ε_0 the permittivity of free space.

We here look for self-consistent solutions of the stationary Vlasov-Poisson system without making assumptions about the order of magnitude of any dimensionless parameter. After defining the normalized radial coordinate $z \equiv r/R$ and the z-dependent quantities,

$$\varphi(z) \equiv \frac{e\phi(r)}{k_BT_e} \ , \ n_{i,e}(z) \equiv \frac{N_{i,e}(r)}{N_\infty} \ , \ n_{em}(z) \equiv \frac{N_{em}(r)}{N_{emp}} \ , \tag{4}$$

Poisson's equation in cylindrical geometry reads

$$\frac{1}{z}\frac{\mathrm{d}}{\mathrm{d}z}\left(z\frac{\mathrm{d}\varphi}{\mathrm{d}z}\right) = -\rho_0^2\left(n_i - n_e - \beta n_{em}\right) \ . \tag{5}$$

Its boundary conditions are $\varphi(z=1) = \varphi_p$ and $\varphi(z \to \infty) \to 0$. Although we have taken single-charged ions for simplicity, yet it is a hypothesis that can be easily relaxed in our model.

As shown below, OMT can be used to write the particle densities $N_\alpha(r) = \int\int f_\alpha(r, v_r, v_\theta) dv_r dv_\theta$ ($\alpha = i$, e, em) as functionals of the electrostatic potential $\phi(r)$, i.e., n_α in Eq. (5) as functionals of $\varphi(z)$. The Vlasov equation conserves the distribution function along particle orbits (Vlasov characteristics), being the same as where they originate. This origin, being infinity for plasma species and the probe for emitted electrons, will be denoted by the subscript 0. Thus, for orbits that can exist at radius r, one has $f_{e,i}(r, \boldsymbol{v}) = f_{Me,i}(\boldsymbol{v}_0)$ and $f_{em}(r, \boldsymbol{v}) = f_{HM}(\boldsymbol{v}_0)$. Otherwise, $f_\alpha(r, \boldsymbol{v}) = 0$. Whether an orbit can exist at r is governed by two other invariants.

Due to the cylindrical symmetry of the problem and its stationary character, the *angular momentum*,

$$J_\alpha = m_\alpha r v_\theta \ , \tag{6}$$

and the *transverse energy*,

$$E_\alpha = m_\alpha(v_r^2 + v_\theta^2)/2 + U_\alpha(r) \ , \tag{7}$$

are all conserved. The potential energy $U_\alpha(r)$ for each species is defined as

$$U_e = -e\phi(r) \ , \ U_i = e\phi(r) \ , \ U_{em}(r) = -e\left[\phi(r) - \phi_p\right] \ . \tag{8}$$

These two constants suffice to characterize particle orbits. They allow to transform the density integration over $v_r v_\theta$-domain to EJ-domain, named D, that aggregates all the orbits present at r. This domain is categorized into two sub-domains, as $D = 2(D_1 + D_2)$, with the factor 2 for considering only positive J hereafter. The sub-domain D_1 stands for the orbits arriving at r for the first time (a, b, and c in Fig. 1) and D_2 for the orbits reflected back to r again (c).

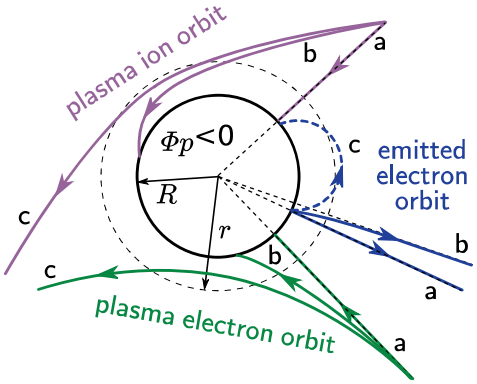

FIG. 1. Diagram of particle orbits around a cylindrical emissive probe. The emitted electron orbit c can only exist in the case of potential dip.

For an orbit to be allowed at r, it is *necessary* (not sufficient) to satisfy simultaneously the following two requirements:

$$E_\alpha \geq U_\alpha(r) \ , \tag{9}$$

$$m_\alpha^2 r^2 v_r^2 = J_{\alpha r}^2(r, E_\alpha) - J_\alpha^2 \geq 0 \text{ for all } E_\alpha \geq U_\alpha(r) \ , \tag{10}$$

where

$$J_{\alpha r}^2(r, E_\alpha) = 2m_\alpha r^2 \left[E_\alpha - U_\alpha(r)\right] \ . \tag{11}$$

That is to say, not only does the energy have to be large enough to overcome the potential-energy hill, $E_\alpha \geq U_\alpha$, but also the angular momentum has to be small enough, $J_\alpha^2 \leq J_{\alpha r}^2$. The *sufficient* condition for an orbit to arrive at r is to satisfy the previous condition along the trajectory at every r' prior to r, yielding the sub-domain D_1 as

$$D_1 = \left\{(E_\alpha, J_\alpha) : \ E_\alpha \geq U_\alpha^*(r), \ J_\alpha \leq J_{\alpha r}^*(r, E_\alpha)\right\} \ , \tag{12}$$

where two auxiliary functions were defined,

$$U^*_{\alpha r}(r) \equiv \max\{U_\alpha(r')\} \ , \ J^*_{\alpha r}(r, E_\alpha) \equiv \min\{J_{\alpha r}(r', E_\alpha)\} \ ,$$
$$R \le r' \le r \text{ for } \alpha = em \ , \quad r \le r' < \infty \text{ for } \alpha = i, e \ .$$

The sub-domain D_2 can be written as $D_2 = D_1 - D_t$, with D_t including the orbits that end at the probe for plasma species and at infinity for emitted electrons (a and b in Fig. 1):

$$D_t = \{(E_\alpha, J_\alpha) : \ E_\alpha \ge U^*_\alpha, \ J_\alpha \le J^*_\alpha(E_\alpha)\} \ , \tag{13}$$
$$U^*_\alpha \equiv \max\{U_\alpha(r') : \ R \le r' < \infty\} \ ,$$
$$J^*_\alpha(E_\alpha) \equiv \min\{J_{\alpha r}(r', E_\alpha) : \ R \le r' < \infty\} \ .$$

After defining $j^2_\alpha \equiv J^2_\alpha/(2m_\alpha R^2 k_B T_\alpha)$, $j^2_{\alpha z}(z, \epsilon_\alpha) \equiv J^2_{\alpha r}(r, E_\alpha)/(2m_\alpha R^2 k_B T_\alpha)$, $u_{\alpha z}(z) \equiv U_{\alpha r}(r)/(k_B T_\alpha)$, and $\epsilon_\alpha \equiv E/(k_B T_\alpha)$, the density integration becomes

$$\begin{aligned} n_\alpha(z) =& H_\alpha \int\int_{D=2(2D_1-D_t)} \frac{\exp(-\epsilon_\alpha)\, \mathrm{d}\epsilon_\alpha\, \mathrm{d}j_\alpha}{2\pi\sqrt{j^2_{\alpha z}(z,\epsilon_\alpha) - j^2}} \\ =& 2H_\alpha \int_{u^*_{\alpha z}(z)}^{\infty} \frac{\exp(-\epsilon_\alpha)}{\pi} \arcsin\frac{j^*_{\alpha z}(z,\epsilon_\alpha)}{j_{\alpha z}(z,\epsilon_\alpha)}\, \mathrm{d}\epsilon_\alpha \\ & - H_\alpha \int_{u^*_\alpha}^{\infty} \frac{\exp(-\epsilon_\alpha)}{\pi} \arcsin\frac{j^*_\alpha(\epsilon_\alpha)}{j_{\alpha z}(z,\epsilon_\alpha)}\, \mathrm{d}\epsilon_\alpha \ , \\ & H_{i,e} = 1 \ , \quad H_{em} = 2 \ . \end{aligned} \tag{14}$$

The temperature ratios, δ_i and δ_p, enter here as $j^2_{\alpha z}(z, \epsilon_\alpha) \equiv z^2[\epsilon_\alpha - u_{\alpha z}(z)]$, where $u_{iz}(z) \equiv \varphi/\delta_i$, $u_{ez}(z) \equiv -\varphi$, and $u_{emz}(z) \equiv -(\varphi - \varphi_p)/\delta_p$. Apparently, the density at z does not only depend on the local potential at z, but also on the values elsewhere.

The substitution of Eq. (14) into Eq. (5) yields a single integro-differential equation for $\varphi(z)$. Once $\varphi(z)$ is computed, other macroscopic quantities can be calculated, such as density profiles from Eq. (14). The currents, contributed by the plasma electrons/ions arriving at the probe and the emitted electrons that reach infinity, are determined by the sub-domain $2D_t$. After being normalized with the electron thermal random current per unit length $I_{th} = 2\pi ReN_\infty\sqrt{k_B T_e/2\pi m_e}$, the currents then read

$$i_\alpha = \frac{2G_\alpha}{\sqrt{\pi}} \int_{u^*_\alpha}^{\infty} j^*_\alpha(\epsilon_\alpha) \exp(-\epsilon_\alpha)\, \mathrm{d}\epsilon_\alpha \ , \tag{15}$$
$$G_i = -\sqrt{\delta_i/\mu_i}, \quad G_e = 1, \quad G_{em} = -2\beta\sqrt{\delta_p} \ ,$$

which is defined positive for collected electron current. Note that the mass ratio $\mu_i \equiv m_i/m_e$ appears naturally in current calculations but not in the Vlasov-Poisson system.

If the potential is monotonic, some classical probe results can be retrieved from Eqs. (14) and (15) without details of $\varphi(z)$. For both emitted and attracted species, at the condition of satisfying both $j^*_\alpha(\epsilon_\alpha) = j_{\alpha z}(1, \epsilon_\alpha)$ and $u^*_\alpha = 0$, their currents (absolute magnitude) achieve the maxima. Once there is no potential dip, emitted electrons from a negatively-biased probe ($\varphi_p < 0$) always meet this condition. As all the electrons reach infinity successfully, this maximum emitted current is the RD current, $i_{em} = -i_{RD} = -2\beta\sqrt{\delta_p}$. For attracted species, ions for $\varphi_p < 0$ and electrons for $\varphi_p > 0$, this maximum current is the OML current. At the OML condition, the current is limited by the barrier $j^*_{\alpha z}(1, \epsilon_\alpha)$ at the probe other than any barrier outside the probe, due to $j^*_{\alpha z}(z, \epsilon_\alpha) \geq j^*_{\alpha z}(1, \epsilon_\alpha)$. The electron-OML ($e$-OML) current is then recovered from Eq. (15) as $i_e = i_{OML}(\varphi_p) = 2\sqrt{\varphi_p/\pi} + \exp(-\varphi_p)\mathrm{erfc}(\sqrt{\varphi_p})$, while the ion-OML ($i$-OML) current is $i_i = -\sqrt{\delta_i/\mu_i} \times i_{OML}(-\varphi_p/\delta_i)$. Regarding densities at the probe, one finds from Eq. (14) a minimum for emitted electrons, $n_{em}(1) = 1$, and the well-known OML result for attracted species, $n_e(1) = 1/2$ [$n_i(1) = 1/2$] for $\varphi_p > 0$ [$\varphi_p < 0$] as a maximum.

III. QUALITATIVE DISCUSSIONS

Before showing quantitative results, we will first anticipate typical operational regimes and explain the reasons underneath. For a cylindrical probe immersed in a plasma with temperature ratio T_i/T_e and biased at ϕ_p, the existence of a maximum probe radius R_{max} for OML collection is well-known, above which the current collection will not be OML. An asymptotic analysis without emission ($I_{RD} = 0$) has found this R_{max} for different T_i/T_e and $e\phi_p/k_BT_e$[15]. As shown by Figs. 6 and 7 in Ref. [15], for an arbitrary T_i/T_e ratio, a minimum radius R^* exists as R_{max} varies with $e\phi_p/k_BT_e$. For $\phi_p > 0$, if $R > R^*$, an OML/non-OML transition is followed by a non-OML/OML transition as ϕ_p increases. Otherwise, for $R \leq R^*$, the electron collection is OML for all $\phi_p > 0$. If electrons and ions have identical temperature ($T_i = T_e$), the radius R^* is the same for both electron collection with $\phi_p > 0$ and ion collection with $\phi_p < 0$. Likewise, the values of $|\phi_p|$ at the transitions, if there are, are also the same for both $\phi_p > 0$ and $\phi_p < 0$. This is because the mass ratio μ_i does not enter the Poisson-Vlasov system. Thus, for a probe with R and $|\phi_p|$, once $T_i = T_e$, the $|\phi(r)|$

profile will be the same, regardless of the sign of ϕ_p. If $T_i \neq T_e$, the R^* and the $|\phi_p|$ values at the transitions would be different for negative and positive probe.

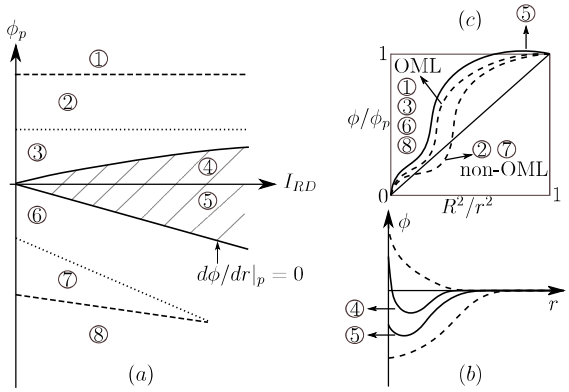

FIG. 2. Panel (a) shows the EP operational regimes: 1) e-OML; 2) e-non-OML; 3) e-OML; 4) non monotonic potential at positive probe bias; 5) non-monotonic potential at negative probe bias; 6) i-OML; 7) i-non-OML; 8) i-OML. Radial potential distribution is qualitatively drawn in two different ways in (b) and (c), with the numbers indicating the correspondent operational regime.

Figure 2a shows the operational regimes for a probe radius that allow all four OML transitions. Theses regimes are enumerated from one to eight, with explanations in the caption. These numbers will be used later in this article as OP-n (OPerational regime - n) for simplicity. For $I_{RD} = 0$, it presents the case without emission as discussed above. For $\phi_p > 0$, because nearly all emitted electrons are reflected back at the immediate vicinity of the probe, negligible emitted-electron space charge renders the two e-non-OML/e-OML transition boundaries varying little with I_{RD}. For $\phi_p < 0$, as shown in Fig. 6 from Ref. [34], thermionic emission increases the R threshold and enlarges the parameter range for OML validity. Consequently, as I_{RD} increases, the i-non-OML region (OP-7) shrinks. There is one moment that the R threshold becomes equal to the actual probe radius. Further increase in I_{RD} results in always OML collection. For this reason, the two bottom transition boundaries meet at certain I_{RD}, creating a closed and reduced i-non-OML region.

The qualitative potential profiles are shown in a r-ϕ plane as in Fig. 2b and in a R^2/r^2-ϕ/ϕ_p plane as in Fig. 2c. When the potential is monotonic (dashed curves), how the *barrier* for attracted-particle collection, $j^*_{\alpha z}(z, \epsilon_\alpha)$, varies with z can be directly observed from Fig. 2c[15] . For instance, for electron collection with $\varphi_p > 0$, as electrons move from infinity to the probe with decreasing z, a decreasing $z^2\varphi$ suffices to have $j^2_{ez}(z, \epsilon_e) = z^2(\epsilon_e + \varphi)$

also decrease. So, if the ordinate-to-abscissa profile ratio in Fig. 2c, $z^2\varphi/\varphi_p$, decreases all the way to the probe, whether an electron orbit can arrive at any z is determined by the local potential there only because of $j^*_{ez}(z,\epsilon_e) = j_{ez}(z,\epsilon_e)$. This situation, where there is no absorption radius for current collection at any z, was considered in[32] as mentioned in Sec. I. If the $z^2\varphi/\varphi_p$ ratio does not monotonically decrease towards the probe, the current collection at z can be limited by a *barrier* $j^*_{ez}(z,\epsilon_e) = j_{ez}(z^*,\epsilon_e)$, i.e., by an *absorption radius* $z^* > z$. For OML collection, $j^*_{ez}(1,\epsilon_e) = j_{ez}(1,\epsilon_e)$ requires that the $z^2\varphi/\varphi_p$ ratio has its global minimum at R, thus the potential profile in Fig. 2c lying above or osculating the diagonal. If this potential profile osculates with the diagonal, this *just-OML* situation has been considered in[34] to find the R_{max}. In the non-OML regime, this potential profile crosses the diagonal. Therefore, the collected current, being limited by a *barrier* away from the probe (or an *absorption radius* $z^* > 1$), will be less than the OML current.

Now let us look at the parametric plot Fig. 2(a) again, with an emission level I_{RD} such that the probe passes all operational regimes as ϕ_p varies. For $\phi_p << 0$, the potential is monotonic [bottom dashed curve in panel (b)]. The probe collects OML ion current [OP-8] as the potential profile lies above the diagonal in panel (c). Increasing ϕ_p leads to i-non-OML [OP-7] regime that is followed by another transition [OP-7/6] to i-OML regime [OP-6]. As ϕ_p increases, the emitted electrons are less accelerated outwards, thus resulting in more negative space charge. How this increased negative space charge affects the potential profile can be directly observed from Poisson's equation. Because the right-hand side of Eq. (5) becomes consequently more positive, the curvature of the potential distribution becomes more negative. For a negative probe bias, this suppresses the inward-pointing electric field near the probe. Then, at certain ϕ_p, the electric field at the probe vanishes, as $\mathrm{d}\phi/\,\mathrm{d}r|_p = 0$ [bottom solid curve in (a)]. Above this boundary, a potential dip builds up [OP-5]. In this non-monotonic regime, the emitted current is SCL, below RD current, and the ϕ/ϕ_p-R^2/r^2 profile in (c) exceeds the square. This potential dip does persist even for some positive ϕ_p [OP-4]. Further increase of ϕ_p, after escaping the shadowed region in (a), yields again a monotonic potential [top dashed curve in (b)]. Two OML transitions [OP-3/2 and OP-2/1] for electron collection then occur for $\phi_p > 0$.

IV. QUANTITATIVE DISCUSSIONS

General quantitative results and the determination of operational regimes require solving the integro-differential equation. Given β, δ_i, δ_p, φ_p, and ρ_0, Eqs. 5 and 14 are solved with a numerical scheme similar to that used in Ref. [16] for LP. The spatial coordinate z is truncated up to a maximum radius z_{max}. In such a finite interval, we introduce a non-uniform mesh and a vector $\boldsymbol{\varphi}$ that encompasses $\varphi(z)$ at all mesh points. We then apply a Newton-Raphson method to solve the nonlinear algebraic equations $\boldsymbol{F}(\boldsymbol{\varphi}) = \boldsymbol{\varphi} - \boldsymbol{\varphi}_{out} = 0$, with $\boldsymbol{\varphi}_{out}$ computed as follows. With an initial guess for $\boldsymbol{\varphi}$, the numerical scheme first computes particle densities at the grid points, by carrying out the integrals in Eq. (14) using a simple Simpson rule. Secondly, using a finite-element formulation, vector $\boldsymbol{\varphi}_{out}$ is found by solving Poisson's equation Eq. (5) with the boundary conditions for cylindrical probes as[35]

$$\varphi|_{z=1} = \varphi_p \tag{16}$$

$$\varphi|_{z_{max}} \propto \frac{1}{z_{\max}} \ , \ \text{i.e.,} \ \left.\frac{\partial\varphi}{\partial z}\right|_{z_{max}} = -\left.\frac{\varphi}{z}\right|_{z_{max}} \ . \tag{17}$$

The most costly part of the algorithm, i.e. the computation of the Jacobian of $\boldsymbol{F}$, is carried out in our code by several processors in parallel.

This numerical algorithm was used to compute the I-V characteristics for an EP with $R \approx 3.6\,\text{mm}$ and $W \approx 2.5\text{eV}$, at several T_p, immersed in an oxygen plasma with $T_i = T_e \approx 0.25\text{eV}$, and $N_\infty \approx 1.07 \times 10^{12}\,\text{m}^{-3}$. The exact solutions were then found, for dimensionless parameters $\delta_i = 1$, $\rho_0 = 1$, $\mu_i = 29164.1$, and $\beta = 3.54 \times 10^{14}\,(\delta_p)^{3/2}\exp(-10/\delta_p)$, for a range of probe bias ($-800 \leq \varphi_p \leq 800$), and for the cases of no emission and $\delta_p = 0.3$, 0.31, 0.32, 0.33, 0.34, which leads to different emission level as $\beta = 0$, 0.19, 0.60, 1.72, 4.63, 11.81, or $I_{RD}/I_{th} = 0$, 0.21, 0.66, 1.94, 5.32, 13.77. This set of parameters was selected according to two criteria. In first place, they correspond to typical plasma parameters in space environment (Low-Earth Orbit), where the collisionless hypothesis of the OMT may apply. In second place, under these parameter ranges, the EP operational regimes presents a parametric diagram as shown in Fig. 2, with two OML/non-OML transitions.

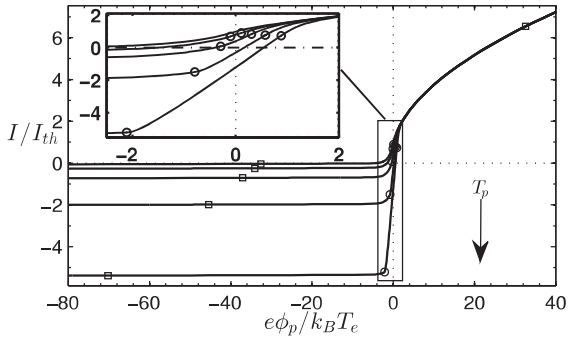

FIG. 3. I-V curves for no emission and $T_p/T_e = 0.3$, 0.31, 0.32, 0.33, with circles and squares for monotonic/non-monotonic and OML/non-OML transitions respectively.

A. I-V Characteristics

The I-V curves for different probe temperatures (except for $\delta_p = 0.34$) are shown in Fig. 3. The probe biases at which the transitions of operational regimes occur are indicated by different markers. Each curve has two square markers and two circle markers, corresponding to the OML/non-OML [OP-2/3, OP-6/7] and the monotonic/non-monotonic [OP-3/4, OP-5/6] transition, respectively. The OP-1/2 and OP-7/8 transitions occur at very high $|\varphi_p|$, thus not shown in Fig. 3. For a certain probe temperature, if the probe is biased at any potential that lies outside the two circles, the resultant potential profile is monotonic. Between the circle and its adjacent square, the collected current is OML.

For high enough positive probe bias, almost all emitted electrons are reflected back at the immediate vicinity of the probe, thus producing negligible space-charge effects. Therefore, all I-V curves coincide as a collecting LP. However, the exact point where they depart from the LP curve is not clear and it depends on the emission level (see Fig. 3 inset). This inhibits the *separation-point* method to be a reliable diagnostic technique, which is congruent with present knowledge about this method[7]. For low enough negative probe bias, all electrons are successfully emitted, with the total current being $I \approx I_{em} = -I_{RD}$, limited by the probe temperature.

Between the circles in Fig. 3, the potential is not monotonic (dashed region in Fig. 2). The self-consistent description of this relevant parametric region is one of the novelties of this work. Due to the retarding electric field that repels back the emitted electrons and yields $I_{em} < I_{RD}$, the emitted electron current reduces rapidly as φ_p increases, i.e., the

total collected (electron) current I increases rapidly. As also shown in Fig. 3, the slope $\mathrm{d}i/\,\mathrm{d}\varphi_p$ steepens with emission and the floating potential φ_f, the probe bias that results in zero current at the probe ($I = 0$), can occur within this non-monotonic regime. In our calculations (shown later), it was observed that potential profiles with potential dips could happen even for $\varphi_f > 0$, as the top solid curve in Fig. 2b. Such a result was also observed in particle-in-cell (PIC) simulations for emitting spheres[2].

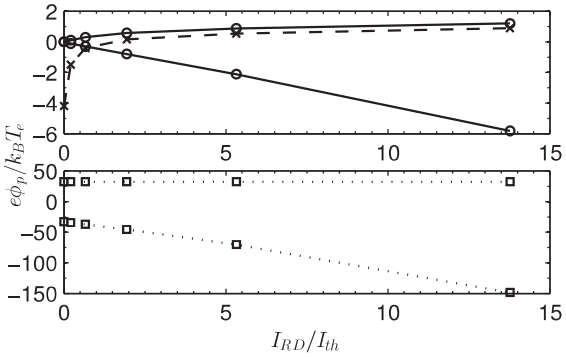

FIG. 4. Parametric plane for monotonic/non-monotonic (solid-circle) and OML/non-OML (dot-square) boundaries and floating potentials (dash-cross).

The boundaries of the different operational regimes in Fig. 3 are presented in Fig. 4 as a function of the normalized probe potential and emission level (φ_p versus I_{RD}/I_{th}). This plot is the quantitative counterpart of Fig. 2, except that the results are shown in two panels to ease the visualization. As anticipated in Fig. 2a, the OML/non-OML boundaries (squares) for $\varphi_p > 0$ are independent of emission while, for $\varphi_p < 0$, emission broadens the φ_p range of OML ion collection. Regarding the monotonic/non-monotonic boundary (circles), it decreases with emission for $\varphi_p < 0$ whereas tends to saturate for $\varphi_p > 0$. The floating potential φ_f is also shown in Fig. 4 and it can be clearly observed that the probe can float in the non-monotonic regime.

B. Potential and Density Profiles

Potential and density profiles at different regimes are now presented for the emission level associated to $\delta_p = 0.31$. For positive probe bias with monotonic potential, results are not shown because they are out of interest here. Also, due to $\delta_i = 1$, at high enough $|\varphi_p|$, the radial potential distribution $|\varphi(z)|$ would be the approximately same for both negative and

positive probe bias. To compare with the case without emission, some of the potential and density profiles without emission are selected to be illustrated by the dash-dot curves in the figures of this section. These dash-dot curves will not be shown in the legends but only explained in the caption.

1. *Monotonic potential with* $\phi_p < 0$

Potential profiles, ϕ/ϕ_p versus R^2/r^2, are shown quantitatively in logarithmic scale in Fig. 5, to present the profile clearly for both $z \to \infty$ and $z = 1$. In the qualitative plot Fig. 2(b), this profile was presented in linear scale, where the variation of the ordinate-to-abscissa profile ratio indicates that of $z^2\varphi/\varphi_p$. Slightly different in logarithmic scale, this variation is indicated by the vertical difference from the profile to the diagonal: $\log(z^2\varphi/\varphi_p) = \log(\varphi/\varphi_p) - \log(1/z^2)$. The condition for OML collection is still to have this profile above the diagonal.

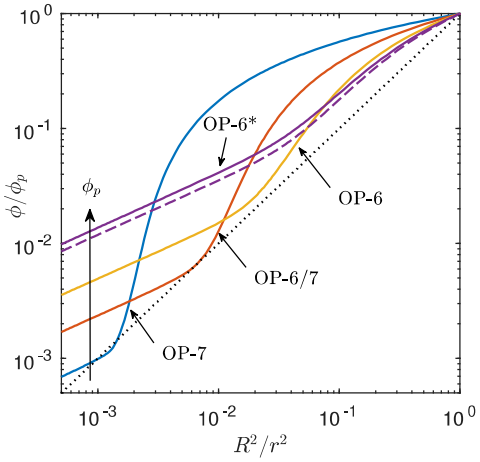

FIG. 5. Potential profiles (ϕ/ϕ_p versus R^2/r^2 in logarithm scale) for $T_p/T_e = 0.31$, $\beta = 0.60$, $T_i/T_e = 1$, $R/\lambda_D = 1$, and $e\phi_p/k_BT_e = -200$ (OP-7), -37 (OP-6/7), -10 (OP-6), and -2 (OP-6*). The curves are labeled with the operational-regime (OP) numbers or the transition boundary, e.g., OP-6/7 (see Fig. 2). The dash-dot curve is shown for $e\phi_p/k_BT_e = -2$ without emission.

For $\varphi_p = -200$ (OP-7), as ions move inwards from infinity, the vertical difference from the profile to the diagonal first decreases and $z^2\varphi/\varphi_p$ thus also decreases. At certain radius, say z_0, $z^2\varphi/\varphi_p$ meets its local minimum. Further inwards, $z^2\varphi/\varphi_p$ first increases then decreases until the probe. Because the profile lies below the diagonal at z_0, the value of $z^2\varphi/\varphi_p$ is

always larger than the local minimum found at z_0. Therefore, for ion collection at any radius between z_0 and the probe, an absorption boundary outside that radius always exists. Due to the absorption boundary, the current collected by the probe is limited by barriers away from the probe, i.e., $j^*_{iz}(1,\epsilon_i) \le j_{iz}(1,\epsilon_i)$, thus non-OML.

At the probe bias $\varphi_p \approx -37$ (OP-6/7), the profile osculates the diagonal and the ion collection is just-OML, i.e., $j^*_{iz}(1,\epsilon_i) = j_{iz}(1,\epsilon_i)$ and $j_{iz}(1,0) = j_{iz}(z_0,0)$. Further increase of φ_p results in OML collection as shown for $\varphi_p = -10$ (OP-6) and $\varphi_p = -2$ (OP-6*). For $\varphi_p = -2$, the probe operates in a special case inside the OML regime. Since $z^2\varphi/\varphi_p$ decreases all the way until the probe, there is no absorption boundary for ion collection at any z, i.e., $j^*_{iz} = j_{iz}$ for all z.

For comparison, solutions were also calculated for the case of no emission at these φ_p values. However, the difference is only distinguishable for $\varphi_p = -2$, as shown by the dash-dot curve. It can be seen that the negative space charge from emitted electrons pushes the potential profile to the left away from the diagonal. This actually explains why emission broadens the parameter range for OML validity[34].

For the density of repelled plasma electrons, due to $j^*_{ez}(z,\epsilon_e) = j_{ez}(z,\epsilon_e) = z\sqrt{\epsilon_e+\varphi}$, $j^*_e(\epsilon_e) = j_{ez}(1,\epsilon_e) = \sqrt{\epsilon_e+\varphi_p}$, $u^*_{ez}(z) = u_{ez}(z) = -\varphi$, and $u^*_e = u_{ez}(1) = -\varphi_p$, it is strictly given by Eq. (14) as

$$n_e(z) = \exp(\varphi) - \int_{-\varphi_p}^{\infty} \frac{\exp(-\epsilon_e)}{\pi} \arcsin\frac{\sqrt{\epsilon_e+\varphi_p}}{z\sqrt{\epsilon_e+\varphi}}\,\mathrm{d}\epsilon_e \ . \tag{18}$$

For $|\varphi_p| \gg 1$, the well-known Boltzmann law is obtained as

$$n_e(z) \approx \exp(\varphi) \ , \tag{19}$$

because the second term in the right-hand side of Eq. (18) is negligible. This approximation also worsens near the probe, with the error becoming $err = \exp(\varphi_p)/2$ at the probe, which is confirmed by the numerical results shown in Fig. 6a.

As the potential is monotonic, the emitted electrons are all the way accelerated towards the infinity. Consequently, looking at the density integration in a form of $\int f\,\mathrm{d}\boldsymbol{v}$, since f is conserved and the integration range is reduced, their density would decrease with z, as shown in Fig. 6(b) where n_{em} decreases from one at the probe to be zero quickly as moving outwards. This density integration Eq. (14) can be estimated, at the region not so close to

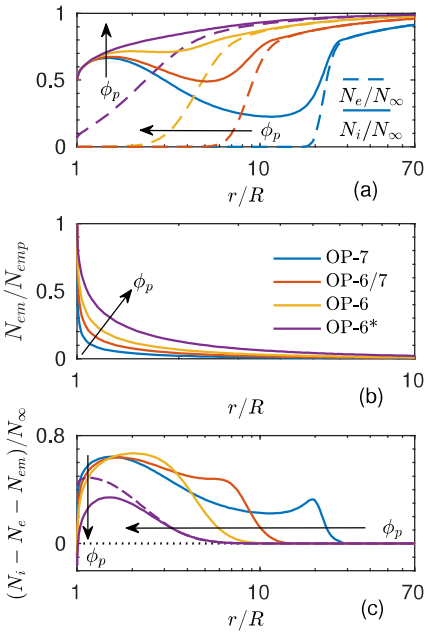

FIG. 6. Density profiles for $T_p/T_e = 0.31$, $\beta = 0.60$, $T_i/T_e = 1$, $R/\lambda_D = 1$, and $e\phi_p/k_BT_e = -200$ (OP-7), -37 (OP-6/7), -10 (OP-6), and -2 (OP-6*). The net density profiles without emission are shown by the dash-dot curves for $e\phi_p/k_BT_e = -2$.

the probe

$$
\begin{aligned}
n_{em}(z) =& 2\int_0^\infty \frac{\exp(-\epsilon_{em})}{\pi} \arcsin \frac{\sqrt{\dfrac{\epsilon_{em}\delta_p}{(\varphi-\varphi_p)}}}{z\sqrt{\dfrac{\epsilon_{em}\delta_p}{(\varphi-\varphi_p)}+1}} \mathrm{d}\epsilon_{em} \\
\approx& 2\int_0^\infty \frac{\exp(-\epsilon_{em})}{z\pi} \sqrt{\frac{\epsilon_{em}\delta_p}{\varphi-\varphi_p}} \mathrm{d}\epsilon_{em} \ , \\
=& \frac{1}{z}\sqrt{\frac{\delta_p}{\pi(\varphi-\varphi_p)}} \ ,
\end{aligned}
\tag{20}
$$

where the conditions $j^*_{emz}(z,\epsilon_{em}) = j^*_{em}(\epsilon_{em}) = j_{emz}(1,\epsilon_{em}) = \sqrt{\epsilon_{em}}$ and $u^*_{emz}(z) = u^*_{em} = u_{emz}(1) = 0$ were used. Alternatively, this expression can also be obtained from fluid description considering all electrons emitted with zero velocity thus moving radially away from the probe. Since the azimuthal velocity decreases due to the conserved angular momentum and the radial velocity increases due to the conserved energy, a radial movement thus approximates well the emitted electrons away from the probe, as seen from orbits a and b in Fig. 1. This approximation of course breaks down near the probe, with an infinite value

at the probe. Also, it is less accurate as $|\varphi_p/\delta_p|$ decreases. Numerical results presented in Fig. 6b show good agreement with this approximation except very near the probe. For instance, evaluated at $z = 2$, this approximation deviates from the numerical result about 0.02 for $\varphi_p = -2$, with a difference being much less than 0.01 for the other three φ_p values. These results verified the validity of using Eq. (20) to approximate emitted-electron densities in the literature[31,32,34].

The plasma ion density is more complicated here because of the orbit motion. As shown in Fig. 6(a), for cases OP-6, OP-6*, and OP-6/7, under OML condition, the ion densities at the probe are found to be 1/2 as predicted. For OP-7 under non-OML condition, the resultant density at the probe is about 0.499, being very close to half. A monotonic behavior in ion density is only observed for the case OP-6*. Under this special condition, due to $j^*_{iz}(z, \epsilon_i) = j_{iz}(z, \epsilon_i) = z\sqrt{\epsilon_i - \varphi/\delta_i}$, $j^*_i(\epsilon_i) = j_{iz}(1, \epsilon_i) = \sqrt{\epsilon_i - \varphi_p/\delta_i}$, and $u^*_{iz}(z) = u^*_i = 0$, the ion density is given by Eq. (14) as

$$n_i(z) = 1 - \int_0^\infty \frac{\exp(-\epsilon_i)}{\pi} \arcsin \frac{\sqrt{\epsilon_i - \varphi_p/\delta_i}}{z\sqrt{\epsilon_i - \varphi/\delta_i}} \, \mathrm{d}\epsilon_i \ , \tag{21}$$

which would decrease all the way to the probe because of a monotonically decreasing $z\sqrt{\epsilon_i - \varphi/\delta_i}$. However, in all the other three cases shown, the ion density does not exhibit a monotonic profile. This emphasizes, not only, the necessity of modeling the ion densities correctly considering orbital motions, but also the necessity of a numerical scheme to carry out complicated calculations for this universal theoretical model.

The net charge at the probe, at OML condition, can be explicitly written out as $n_i(1) - n_e(1) - \beta n_{em}(1) = 1/2 - \exp(\varphi_p)/2 - \beta$. Thus for $\beta = 0.6$, a negative-space-charge region will definitely appear next to the probe. As shown in Fig. 6(c), a double sheath is thus formed and a radius with zero net charge separates two oppositely-charged regions. As φ_p increases, space-charge effects increase too and the zero-net-charge radius moves away from the probe. To compare with no emission, the net density for $\varphi_p = -2$ without emission are shown by the dash-dot curves. It seems that after some distance away from the probe, the with-emission and without-emission curves coincide with each other, as the effects of the emitted electrons are shielded out hereafter.

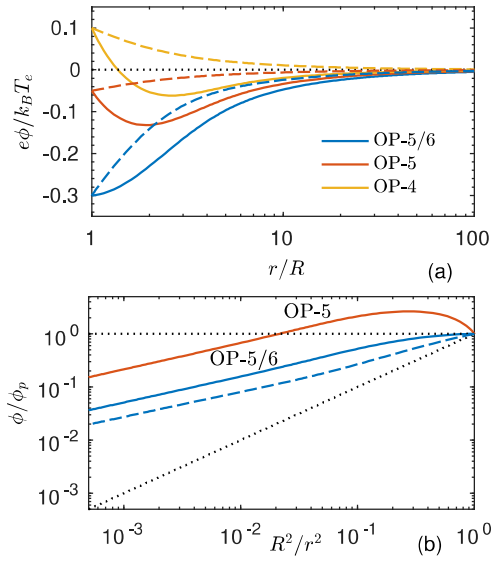

FIG. 7. Potential profiles for $T_p/T_e = 0.31$, $\beta = 0.60$, $T_i/T_e = 1$, $R/\lambda_D = 1$, and $e\phi_p/k_BT_e = -0.3$ (OP-5/6), -0.05 (OP-5), 0.1 (OP-4). The dash-dot curves are shown for profiles under same probe bias, but without emission. In panel (b), no-emission case is only presented for $e\phi_p/k_BT_e = -0.3$.

2. *Non-monotonic potential,* $\varphi_p < 0$

With φ_p increasing, the electric field was found to vanish at $\varphi_p = -0.3$ [OP-5/6 in Fig. 7]. The potential profile in ϕ/ϕ_p-R^2/r^2 plane is tangential to the $\phi/\phi_p = 1$ line at $r = R$. Further increase of φ_p results in a retarding electric field for emitted electrons and a potential dip starts to build up. The potential distribution is no longer monotonic [OP-5 in Fig. 7(a)] and the ϕ/ϕ_p-R^2/r^2 profile exceeds the square [OP-5 in Fig. 7(b)]. This non-monotonic potential does not occur if there is no emission, as shown by the dash-dot curves.

When the potential is no longer monotonic, the density integration in Eq. (14) becomes even more complicated and only numerical methods can shed light on the insight of the space-charge structure and their influences on the potential distribution. As emitted electrons are repelled back by the potential dip, this in turn increases the electron-space-charge near the probe. Consequently, the density ratio N_{em}/N_{emp} becomes large than one near the probe [OP-5 in Fig. 8(b)]. Plasma ions are attracted until the potential minimum and repelled between the minimum and the probe, vice versa for plasma electrons. The disparity between their densities for monotonic potential, as observed in Fig. 6(a), is no longer present [Fig. 8(a)]. This suggests that a pure electron sheath, at least between the potential mini-

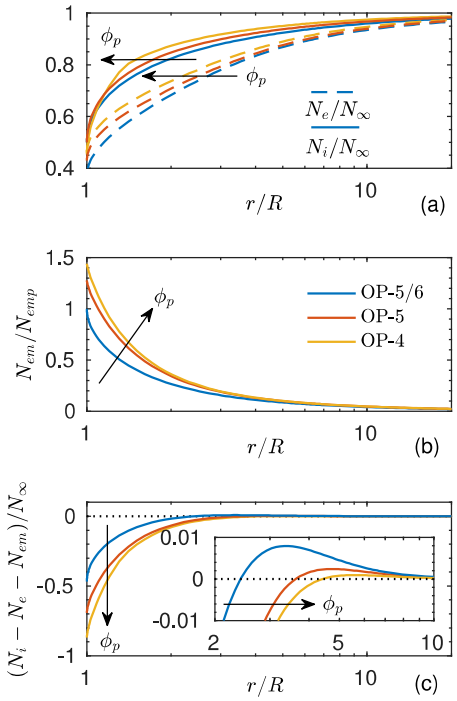

FIG. 8. Density profiles for $T_p/T_e = 0.31$, $\beta = 0.60$, $T_i/T_e = 1$, $R/\lambda_D = 1$, and $e\phi_p/k_BT_e = -0.3$ (OP-5/6), -0.05 (OP-5), 0.1 (OP-4).

mum and the probe, can be a good approximation as used in[31]. As the probe bias increases, more negative space charge accumulated in the region next to the probe, which pushes the zero-net-charge radius much further away from the probe [see inset in Fig. 8(c)].

The effects of these negative space charges can be observed in Fig. 7 by comparing the non-monotonic potential profiles with the dash-dot curves with no emission. In panel (a), if there is no emission, a pure positive-charge sheath results in a positive curvature. With emission, due to the negative net space charge next to the probe, the curvature of the potential becomes negative there. But the potential profile joins the quasi-neutral plasma with a positive curvature due to the positive net charge away from the probe. Again, in panel (b), it can be found that emission pushes the profile away from the diagonal, thus helping the OML collection of ions.

3. Non-monotonic potential with $\phi_p > 0$

If the probe is positively biased and there is no emission, the potential distribution is monotonic as shown by the dash-dot curves in Fig. 7 for $\varphi_p = 0.1$. This positive-potential

sheath attracts electrons and repels ions, leading to negative net space charge everywhere and a resultant negative curvature in potential distribution.

If there is emission and the positive φ_p is not large enough to repel enough emitted electrons back to the probe, then an interesting potential profile is developed. To recover the quasineutrality in plasma, a potential minimum φ_m has to build up so that the net potential drop $\varphi_p - \varphi_m > \varphi_p$ is sufficiently large to repel emitted electrons back to the probe. This potential minimum not only does build up a higher potential energy hill for electrons to climb up but also attracts ions to assure a consistent sheath structure. As shown in Fig. 7 for $\varphi_p = 0.1$, the non-monotonic potential does persist for this positive probe bias. And, instead of being a pure negative-electron sheath, it is again a double sheath with a negative-charge region next to the probe and a positive-charge region extending to the quasineutral plasma [see Fig. 8].

C. Floating Potential

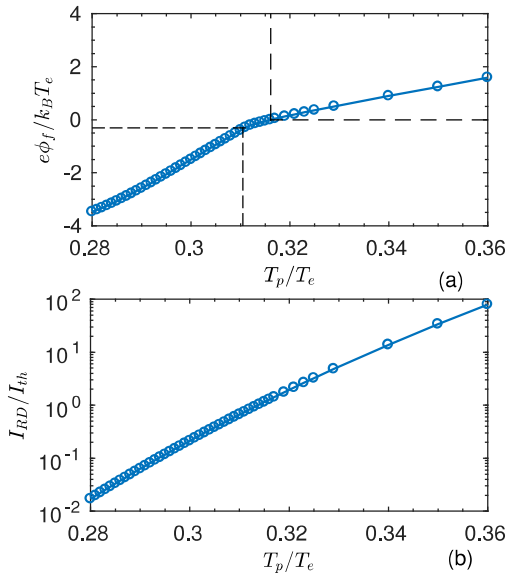

FIG. 9. Normalized floating potential φ_f and the RD-thermal current ratio I_{RD}/I_{th} for a thermionic material with $W = 2.5$eV at different temperature δ_p. The intersections of two dash-point lines and two dashed lines represent the vanished-electric-field condition and the plasma-potential condition respectively.

The most common method to obtain the plasma potential using EPs is the *floating-*

potential technique. To discuss this technique, our numerical scheme was modified to include the floating-probe condition, i.e. the probe bias was considered as an additional unknown and we added the equation $I = 0$. Thus the floating potential $\varphi_f = e\phi_f/k_B T_e$ for different δ_p can be directly calculated, which is shown in Fig. 9(a) for $\delta_p = 0.28$ to 0.36, i.e., the current ratio $I_{RD}/I_{th} \approx 0.02$ to 79.13 [see Fig. 9(b)] for a thermionic material with $W = 2.5$eV.

In Ref. [22], Hobbs and Wesson calculated the floating potential of a planar wall at large emission to be $\varphi_f \approx -1$. However, this is not necessarily applicable for EPs. The OMT results from our calculations show that the probe can float at $\phi_f > 0$, in agreement with simulations for planar geometry[27]. Also, similar to that obtained from PIC simulations for spheres[28], the saturation of floating potential is not clearly observed as in Fig. 9(a). As explained below, this discrepancy can result from two reasons.

First of all, the planar-sheath assumption can fail for cylindrical EP when the sheath thickness is much larger than the probe radius. As shown by the potential profiles in Fig. 10(c), the quasineutrality is recovered even further than a radius that is ten times as the probe radius. As a result, cylindrical geometry is necessary to be properly modelled and studied, as one of the goals of this work.

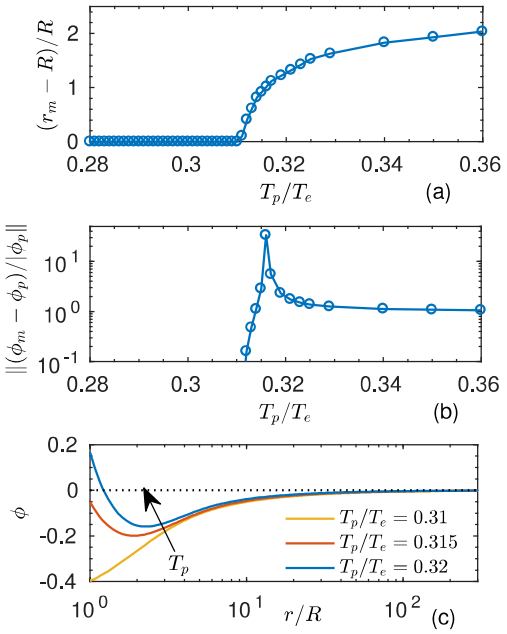

FIG. 10. At the floating potential found for an cylindrical emitter with $W = 2.5$eV at different temperatures: (a) and (b), the minimum potential and its location; (c) potential profile for $\delta_p = 0.31$, 0.315, 0.32.

Secondly, the vanished electric field at the probe surface, $\mathrm{d}\varphi/\,\mathrm{d}z|_{z=1} = 0$, which was imposed to imply the saturation[22], is not a valid assumption for large emission. This assumption would be reasonable if the space charge effect is not strong, so that the potential dip is close to the probe, $r_m - R \ll R$, and with a value close to that of the probe bias, $\varphi_m \approx \varphi_p$. As marked by the intersection of the two dash-point lines in Fig. 9(a), the emitter will start to float with a non-monotonic potential for $\delta_p > 0.311$ [see Fig.10(c)]. As emission increases, the potential minimum can locate at a radius that is comparable with R [see Fig. 10(a)]. Although not shown here, the potential difference between the minimum and the probe, $|\varphi_m - \varphi_p|$, is also found to increase with emission, as expected to repel more emitted electrons back to the probe. To compare this difference with the probe bias, the $|(\varphi_m - \varphi_p)/\varphi_p|$ ratio is plotted in Fig. 10(b), which can be as large as ten (at least). As a result, the potential dip is clearly not negligible and a rigorous theory to investigate this non-monotonic profile is necessary, as the intention of this work.

As shown by the intersection of the two dashed lines in Fig. 9(a), for $\delta_p \leq 0.316$, the probe floats at a negative bias. Accordingly, in Fig. 10(b), the $|(\varphi_m - \varphi_p)/\varphi_p|$ ratio increases with φ_p. At some emission level for $0.316 < \delta_p < 0.317$, the probe would float at zero bias, with $|(\varphi_m - \varphi_p)/\varphi_p|$ thus being infinitely large. Further increase in emission gradually reduces the $|(\varphi_m - \varphi_p)/\varphi_p|$ ratio to one.

Although there is no clear floating-potential saturation, Fig. 9(a) is similar to the experiment curve (Fig. 4 in Ref. [29]). Increasing the emission from no emission, the floating potential first rises rapidly. A sharp decrease of this slope occurs after the probe floats in the non-monotonic regime. Our calculations shows that OMT predicts this transition of operational regime at $\varphi_f \approx -0.31$. This indicates that, if we estimate the plasma potential by looking for the knee in Fig. 9(a), the plasma potential is underestimated with an error about $-0.31T_e$ under the condition considered in this work.

V. CONCLUSIONS

This work presented the *Orbital Motion* Theory (OMT) for cylindrical emissive probes (EPs). Conservation laws have been used to find the particle densities as functionals of the electrostatic potential and then write the Poisson equation as a single integro-differential equation. It unifies in a compact framework for both Langmuir and emissive probes and

predict rigorously and self-consistently the EP characteristics for arbitrary parameter values. For given plasma parameters, probe radius, and probe temperature, the implemented numerical methods typically needs just few seconds or less to solve the integro-differential equation. Such a short time permits to create a broad database for I-V characteristics and floating potential φ_f, parametrized by δ_i, δ_p, ρ_0, and β. As successfully applied nowadays for LPs[19], plasma parameters, in addition to plasma potential, could possibly be found by an appropriate fitting of experimental EP measurements to this numerically generated database. This, in addition to the organization of the operation regimes of EPs in the probe bias-emission level plane, is the major application of the model. The theory can also be used as a benchmark case to validate more complex codes that would relax some of the hypotheses of the OMT.

The theory relies on a set of hypotheses that, although widespread in theoretical works on probe theory, can possibly bring up difficulties in the interpretation of experimental I-V curves. One of them, the Maxwellian plasma assumption faraway from the probe could be easily relaxed. Other distribution functions that would depend on just the energy could be incorporated to the theory by changing the functions inside the integrals of Eq. (14) accordingly. Removing other assumptions is more problematic because they inevitably leads to the breaking of a conservation law. For instance, collisions, flowing plasmas, non-stationary trapping, and probe end effects preclude the conservation of the distribution function, the angular momentum, the energy, and the axial velocity v_z, respectively. The quantitative impact on the collected current of these effects requires computationally demanding algorithms. Studies on trapped-particle effects using a direct Vlasov code[36] are in progress.

However, the results from OMT can be used to test *a posteriori*, whether these assumptions are reasonable or not. For instance, the collisionless hypothesis can be examined by comparing the overall mean free path for electrons, with the sheath radius that can be found from the radial potential and density profiles calculated by the OMT. Similarly, the magnetic effects can be negligible if the electron thermal gyroradius is larger than both R and λ_{De}[15]. The 2-dimensional-probe hypothesis is valid if the probe length is larger than the sheath radius. These criteria are useful only for qualitative estimations and may help to make a correct use of the theory. Nevertheless, the hypotheses of the OMT normally holds in collisionless space plasmas and low pressure laboratory plasmas, which are practical and interesting matters of study.

ACKNOWLEDGMENTS

Work by G. Sánchez-Arriaga was supported by the Ministerio de Economía y Competitividad of Spain (Grant No RYC-2014-15357).

REFERENCES

[1]S. Robertson, Plasma Phys. Controlled Fusion **55**, 093001 (2013).

[2]G. L. Delzanno, G. Lapenta, and M. Rosenberg, Phys. Rev. Lett. **92**, 035002 (2004).

[3]B. Thiebault, A. Hilgers, E. Sasot, H. Laakso, P. Escoubet, V. Genot, and J. Forest, J. Geophys. Res. A **109**, A12207 (2004).

[4]P. Stangeby and G. McCracken, Nucl. Fusion **30**, 1225 (1990).

[5]D. Sydorenko, I. Kaganovich, Y. Raitses, and A. Smolyakov, Phys. Rev. Lett. **103**, 145004 (2009).

[6]J. D. Williams, J. R. Sanmartin, and L. P. Rand, IEEE T. Plasma Sci. **40**, 1441 (2012).

[7]J. P. Sheehan and N. Hershkowitz, Plasma Sources Sci. Technol. **20**, 063001 (2011).

[8]B. Liebig and J. W. Bradley, Plasma Sources Sci. Technol. **22**, 045020 (2013).

[9]Y. Zhang, C. Charles, and R. Boswell, Plasma Sources Sci. Technol. **25**, 015007 (2016).

[10]I. Langmuir and K. B. Blodgett, Phys. Rev. **22**, 347 (1923).

[11]H. M. Mott-Smith and I. Langmuir, Phys. Rev. **28**, 727 (1926).

[12]S. Lam, Phys. Fluids **8**, 73 (1965).

[13]I. B. Bernstein and I. N. Rabinowitz, Phys. Fluids **2**, 112 (1959).

[14]J. G. Laframboise, "Theory of spherical and cylindrical langmuir probes in a collisionless, maxwellian plasma at rest," Tech. Rep. (University of Toronto Institute for Aerospace Studies, 1966) UTIAS Report, No. 100.

[15]J. R. Sanmartin and R. D. Estes, Phys. Plasmas **6**, 395 (1999).

[16]G. Sanchez-Arriaga and J. R. Sanmartin, Phys. Plasmas **19**, 063506 (2012).

[17]J. E. Allen, R. L. F. Boyd, and P. Reynolds, Proc. Phys. Soc. London, Sect. B **70**, 297 (1957).

[18]F. F. Chen, J. Nucl. Energy, Part C **7**, 47 (1965).

[19]F. F. Chen, Phys. Plasmas **8**, 3029 (2001).

[20]I. Langmuir and K. B. Blodgett, Phys. Rev. **24**, 49 (1924).

[21]I. Langmuir, Phys. Rev. **33**, 954 (1929).

[22]G. D. Hobbs and J. A. Wesson, Plasma Physics **9**, 85 (1967).

[23]M. Y. Ye and S. Takamura, Phys. Plasmas **7**, 3457 (2000).

[24]J. P. Sheehan, N. Hershkowitz, I. D. Kaganovich, H. Wang, Y. Raitses, E. V. Barnat, B. R. Weatherford, and D. Sydorenko, Phys. Rev. Lett. **111**, 075002 (2013).

[25]L. A. Schwager, Phys. Fluids B **5**, 631 (1993).

[26]M. D. Campanell, A. V. Khrabrov, and I. D. Kaganovich, Phys. Rev. Lett. **108**, 255001 (2012).

[27]M. D. Campanell and M. V. Umansky, Phys. Rev. Lett. **116**, 085003 (2016).

[28]G. L. Delzanno and X.-Z. Tang, Phys. Rev. Lett. **113**, 035002 (2014).

[29]R. F. Kemp and J. M. Sellen, Rev. Sci. Instrum. **37**, 455 (1966).

[30]A. Fruchtman, D. Zoler, and G. Makrinich, Phys. Rev. E **84**, 025402 (2011).

[31]K. W. Chang and G. K. Bienkowski, Phys. Fluids **13**, 902 (1970).

[32]J. J. Schuss and R. R. Parker, J. Appl. Phys. **45**, 4778 (1974).

[33]S. Robertson, IEEE T. Plasma Sci. **40**, 2678 (2012).

[34]X. Chen and J. R. Sanmartin, Phys. Plasmas **22**, 053504 (2015).

[35]J. G. Laframboise and L. W. Parker, Phys. Fluids **16**, 629 (1973).

[36]G. Sanchez-Arriaga and D. Pastor-Moreno, Phys. Plasmas **21**, 073504 (2014).